Influence of a target on the electric field profile in a kHz atmospheric pressure plasma jet with the full calculation of the Stark shifts

Journal of Applied Physics

Influence of a target on the electric field profile in a kHz atmospheric pressure plasma jet with the full calculation of the Stark shifts

Cite as: J. Appl. Phys. **125**, 043303 (2019); https://doi.org/10.1063/1.5075544
Submitted: 23 October 2018 . Accepted: 04 January 2019 . Published Online: 23 January 2019

Marlous Hofmans, and Ana Sobota

Journal of Applied Physics ARTICLE scitation.org/journal/jap

Influence of a target on the electric field profile in a kHz atmospheric pressure plasma jet with the full calculation of the Stark shifts

Cite as: J. Appl. Phys. **125**, 043303 (2019); doi: 10.1063/1.5075544
Submitted: 23 October 2018 · Accepted: 4 January 2019 ·
Published Online: 23 January 2019

Marlous Hofmans and Ana Sobota

AFFILIATIONS

EPG, Eindhoven University of Technology, Postbus 513, 5600 MB Eindhoven, The Netherlands

ABSTRACT

The electric field in the head of the plasma bullet (ionization wave) in a cold atmospheric pressure plasma jet is measured using the Stark polarization spectroscopy technique, a noninvasive method. The jet is driven by 1μs long voltage pulses at 6 kV amplitude and 5 kHz frequency, and a helium gas flow of 1.5 slm. Two helium lines (447.1 nm and 492.2 nm) are studied, from which the peak-to-peak wavelength difference between the allowed and forbidden band of the spectral lines is determined. The full derivation to obtain the electric field from this peak-to-peak difference is included in this paper. The electric field is determined both inside and outside the capillary of the jet, up to about 2 cm in the effluent of the jet. Measurements are performed on the freely expanding jet, but especially the influence is studied when a target is placed in front of the plasma jet. Targets with different properties are used: insulating (polyvinyl chloride, PVC), conducting (copper), liquid (distilled water and saline), and organic (chicken breast). It is found that a target changes the electric field of the plasma jet and thus changes the plasma itself. This change depends on the dielectric constant or conductivity of the target: a higher dielectric constant or higher conductivity yields a higher electric field. For a low dielectric constant ($\epsilon_r \approx 3$), the change in the electric field is negligible. Decreasing the distance between the target and the capillary to below 2 cm yields an increase in the electric field.

I. INTRODUCTION

The field of plasma medicine focuses on the use of plasma technology in the treatment of living cells, tissues, and organs.[1] Examples of biomedical applications are wound healing, infection control, and cancer treatment.[2] For this purpose, an atmospheric-pressure plasma jet is used that has a gas temperature of 25–40 °C.[3] The low gas temperature is needed because the plasma jet interacts with sensitive biological systems.

For these applications as well as for all other kinds of surface treatments and for modeling and optimization of the plasmas, it is important to know the parameters of the plasma, such as gas temperature, electron temperature, and density. Multiple spectroscopic methods based on, for example, line width and line intensity have been developed to obtain these parameters from atomic spectra.[4–7] Another important parameter is the macroscopic electric field that is formed at the head of the plasma bullet in the plasma jet. The characteristics of the electric field, among which is the space and time evolution of the electric field, commonly determine the energy and flux of the charged particles in the plasma and thus determine the behavior of the discharge.[8] Therefore, it is essential to know the electric field inside the plasma jet, especially when it is interacting with a target. Measuring the electric field however is not trivial, since the plasma is influenced when, for example, a Langmuir probe is placed near or inside the plasma jet.

Existing methods for measuring the electric field in atmospheric pressure plasmas are CARS based four wave mixing,[9–12] that can only be applied to nitrogen or requires a picosecond laser, second harmonic generation[13,14] that also requires a picosecond laser, laser-collision induced fluorescence[15,16] that requires a kinetic collisional model, measurements based on the Pockels effect[17,18] that yields only the field inside the target, and the intensity ratio of helium lines method[19] that requires a valid collisional-radiative model. The method in this study that is based on optical emission spectroscopy, however, can be applied to the plasma jet without these constraints.

Kuraica *et al.* have developed a method, based on calculations done by Foster,[20] to measure the electric field of a

plasma, using passive emission spectroscopy and the Stark effect.[21–24] Their method has already been applied to, for example, a glow discharge[22,23] and a plasma jet.[25] The method used in this project is a combination of the method of Kuraica *et al.* and the calculations of Foster and it is applied to a pulsed helium plasma jet in interaction with targets of different electrical properties. The details of the calculations can be found in Appendix A. In this paper, we show that the target has a profound influence on the electric field profile of the effluent of the plasma jet.

II. EXPERIMENTAL SETUP AND SPECTRAL ANALYSIS

A. Experimental setup

The atmospheric plasma jet that is used in this study is the same as in previous experiments[3,17,26] and is operated vertically downwards. It consists of a dielectric tube made from pyrex, with a hollow, stainless steel anode inside and a copper ring as the cathode around it, as is shown in Fig. 1(a). The jet is powered by a 1 μs square pulse with a frequency of 5 kHz and an amplitude of 6 kV, created by a function generator (Agilent 33220A), a high voltage power supply (Spellman UHR10P60/CL/220), and a high voltage pulse generator (DEI PVX-4110) as can be seen in Fig. 1(b). The voltage and current of the plasma are measured with a high voltage probe (LeCroy PHV4-3432 14 kV AC) and a Rogowski coil (Pearson Current Monitor 6585) and their signals are monitored on an oscilloscope (LeCroy waveRunner 6100A 1 GHz [dual 10 GS/s, quad 5 GS/s)]. Typical current and voltage signals are shown in Fig. 2. From these signals, the energy per pulse is calculated according to the method described by Sobota *et al.*[27] The helium (purity 5.0) gas flow into the hollow anode is monitored by a Bronkhorst High Tech flow controller and set to a value of 1.5 slm. The used gas line is made of stainless steel to reduce the amount of impurities in the helium flow.

An $f = 150$ mm plano-convex lens (diameter 2.5 in.) is used to focus the emitted light of the plasma jet on the slit of the spectrometer (Jobin Yvon HR 1000 $f = 1$ m, with a 1200 g/mm grating). The slit has a width of 50 μm, yielding an instrumental broadening (full width at half maximum) of 0.067 nm (Gaussian profile). The Van der Waals ($\propto 10^{-3}$ nm), pressure ($\propto 10^{-3}$ nm), Doppler ($\propto 10^{-3}$ nm), natural ($\propto 10^{-6}$ nm)', and Stark ($\propto 10^{-7}$ nm) broadening mechanisms give negligible values, but resonance broadening (0.12 nm, Lorentz profile) cannot be neglected. Together with the instrumental broadening, this yields a Voigt profile line broadening of 0.15 nm.

A linear polarizer is placed just in front of the slit to make sure only linearly polarized light can pass and thus, as is explained in Appendix B, only the axial electric field is measured. The outgoing light of the spectrometer is captured by an iCCD camera (4QuickEdig Stanford Computer Optics). To increase the signal to noise ratio, the camera is cooled by a water cooled Peltier element, maintaining a temperature of 3 °C–4.5 °C.

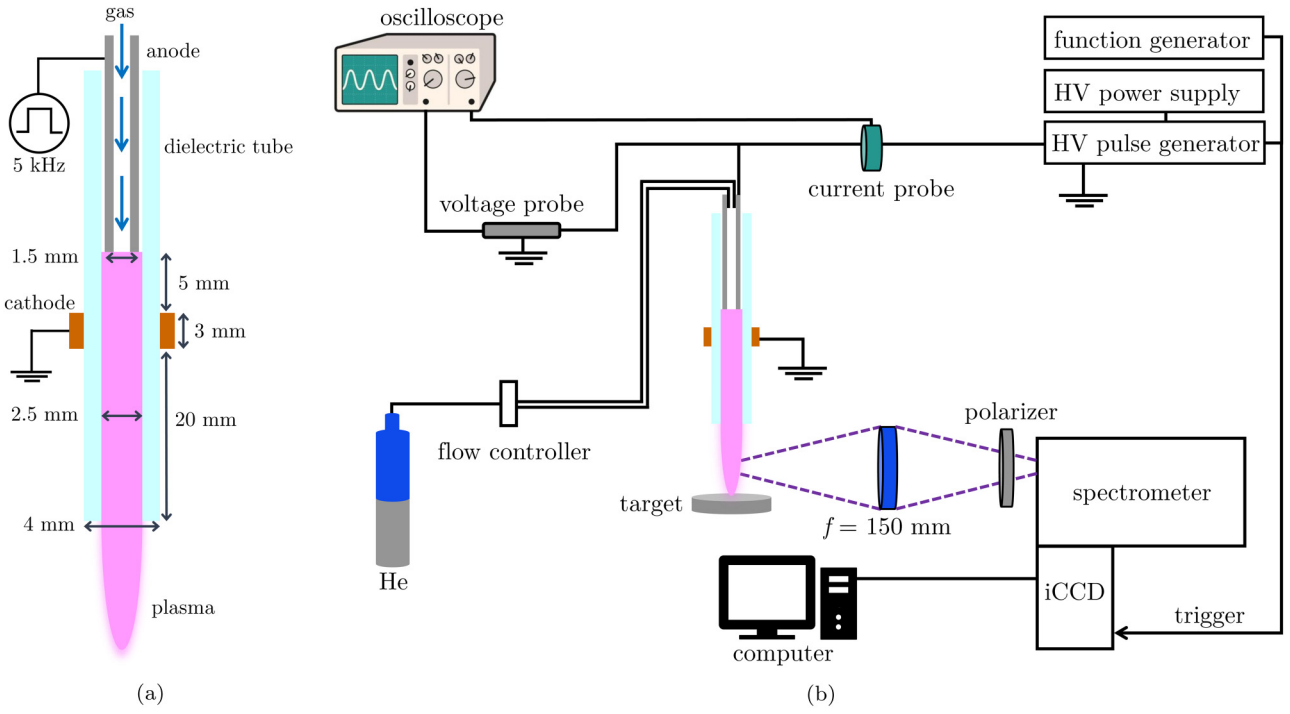

FIG. 1. Schematic overview of (a) the plasma jet and (b) the experimental setup.

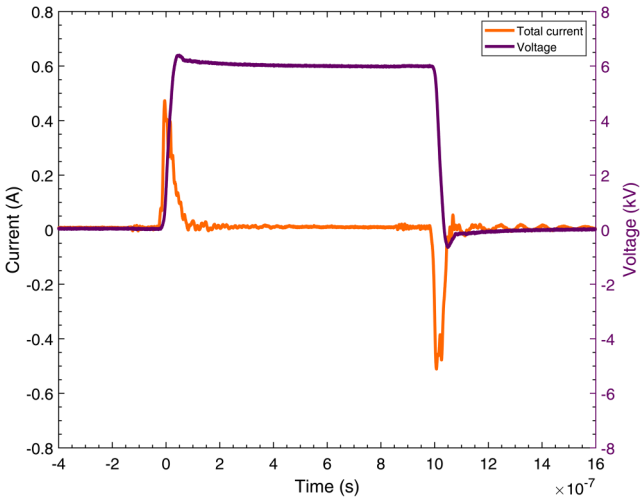

FIG. 2. The total current and voltage signal of one pulse as function of time.

Depending on the intensity of the light, each recorded image contains 10 accumulations, each with 5000-50 000 gates of 200 ns. The gate is triggered at the up-going edge of the pulse signal, with a tunable delay. The CCD chip has a size of width × height = 782 × 582 pixels, yielding a spectral resolution of 0.0135 nm/pix and a spatial resolution of 0.02 mm/pix. Since this height is too low to image the full trajectory of the traveling bullet at once, the bullet is followed both in space and in time. The plasma jet, together with the target, is moved vertically upwards to capture a certain region of the jet on the slit of the spectrometer, until the full jet is imaged. Meanwhile, the delay time of the gate is increased accordingly, to make sure the image of the bullet is captured at the moment it is passing the current observed region of the jet. Even with a long exposure of 200 ns, we only get the data from the head of the bullet as it propagates through space, since the strongest light emission comes from the head. Therefore, the results of long exposures are equivalent to time-resolved measurements, as shown by Sobota *et al.*[3]

Measurements are performed both on the plasma inside the capillary and on the plasma outside the capillary [see Fig. 1(a)]. The latter part is called the plasma plume or the effluent of the jet. Different targets are placed underneath the jet to study the influence of the target on the electric field. A non-conducting target (plastic, PVC) and a conducting target (copper) are used, as well as distilled water, saline (19 g/l NaCl diluted in distilled water), and chicken breast, since they compare better to targets that are used in biomedical applications. The piece of chicken breast was approximately 100 g and presented a piece of tissue of large volume compared to the size of the plasma. Therefore, it is close to actual conditions in a clinic. The liquid targets and the chicken breast are placed in a Petri dish before situating them underneath the plasma jet. All targets were placed on a thin plastic stand, with the grounded table being 20–30 cm below and all other metallic surfaces were kept at least 10 cm away from the jet and the target. Measurements are performed both with and without grounding the conductive targets, and also the effect of different distances between the target and the capillary is examined.

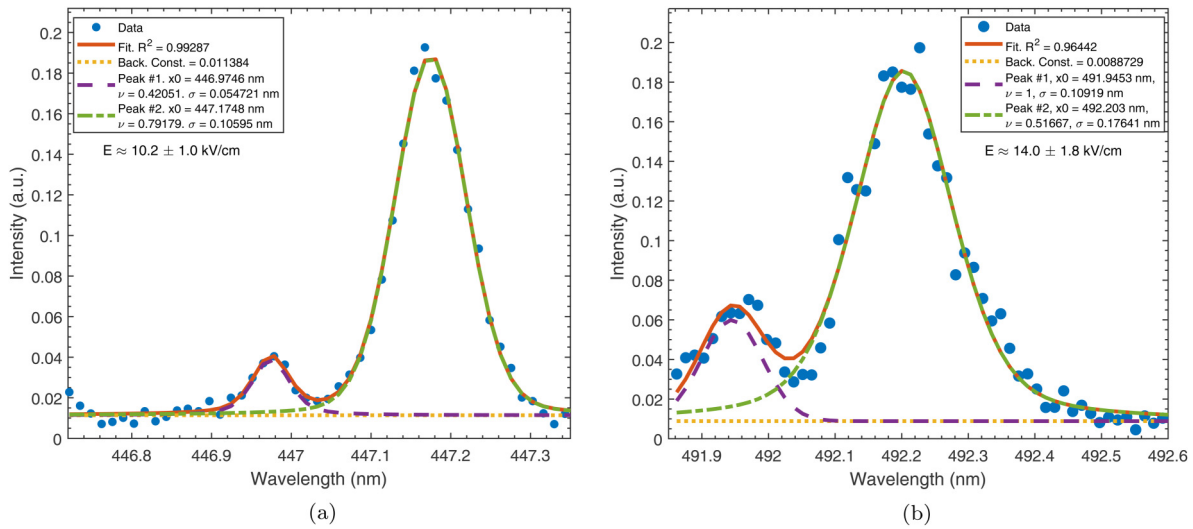

FIG. 3. Example of a fit for (a) the 447.1 nm line and (b) the 492.2 nm line of the forbidden (#1) and allowed (#2) peak, showing the data, the fits and the corresponding electric field strength. x_0 is the position of the peak, ν the Voigt shape of the fit (Lorentz = 0, Gauss = 1), and σ the width of the peak.

B. Spectral analysis

From each recorded image, the spectra are read out by averaging spatially (vertically) over 50 pixels. Within a domain of 0.6–0.7 nm around the observed helium lines, the intensity profile is fitted with Voigt-profiles[28] for the two peaks. Examples of such fits are shown in Fig. 3 for both helium lines. From the distance between the position of the allowed and the forbidden peak, the electric field is calculated.

In order to do this, a theoretical calculation is performed to obtain the energy levels of helium in an external electric field. A combination is made of the calculations done by Foster[20] and Kuraica *et al.*[22] To the authors' knowledge, a calculation with a full derivation has not been published yet. For the sake of reproducibility of the experiment, but also to explain all assumptions in the theory, the full derivation is presented in Appendix A. Here, only the resulting relations will be given.

Two lines of the atomic helium (He I) spectrum will be examined, namely, the 492.2 nm line and the 447.1 nm line. For the He I 492.2 nm line, which has an allowed transition $1s4d\,^1D \rightarrow 1s2p\,^1P^o$ and a forbidden transition $1s4f\,^1F^o \rightarrow 1s2p\,^1P^o$, the difference between the shifted allowed and forbidden component is given by

$$\Delta\lambda_{AF} = -5.2140 \cdot 10^{-6}E^3 + 3.9844 \cdot 10^{-4}E^2 + 0.0058E + 0.1226, \quad (1)$$

with $\Delta\lambda_{AF}$ in nm and E in kV/cm. The He I 447.1 nm line has an allowed transition $1s4d\,^3D \rightarrow 1s2p\,^3P^o$ and a forbidden transition $1s4f\,^3F^o \rightarrow 1s2p\,^3P^o$, yielding

$$\Delta\lambda_{AF} = -3.9620 \cdot 10^{-6}E^3 + 3.4558 \cdot 10^{-4}E^2 + 0.0025E + 0.1433. \quad (2)$$

The electric field in the experiment is obtained by numerically solving the above equations for E with the measured wavelength difference substituted for $\Delta\lambda_{AF}$.

III. RESULTS AND DISCUSSION

The total, discharge, and capacitive energy per pulse of the plasma jet is shown in Fig. 4(a) for the freely expanding jet and for the jet impinging on the different targets, placed at a 1 cm distance. It can be seen that the capacitive energy is quite the same for all targets and without a target. This confirms the expectations, since the capacitive energy is mainly determined by the equipment in the electrical circuit, which remains the same during the experiments, and not by the plasma itself. The discharge energy, and thus the total energy which is the sum of the discharge and the capacitive energy, is mainly determined by the plasma and therefore these energies change with the different targets. When the target is grounded, these energies increase because more charge can be dissipated and thus more charge is present in the channel between the jet and the target.

The measured electric field is the macroscopic field at the front of the ionization wave, where light emission takes place and the electric field is the highest. Figure 4(b) shows the electric field in the freely expanding jet as a function of the distance from the anode, for measurements at the two different helium lines. The error-bars are calculated as follows. Five consecutive measurements are performed and for each measurement the spectrum is fitted, yielding a distance between the allowed and forbidden peak plus an error that indicates the minimum and maximum distance between the peaks. The minimum is taken as the lower bound error on the electric field and the maximum as the upper bound error. The displayed error in the figure is then the average of these errors over the five measurements and over the data points if

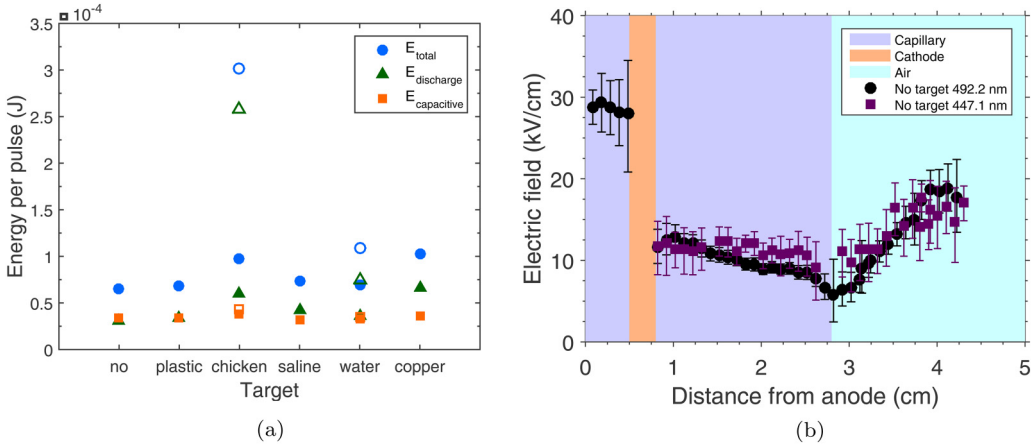

FIG. 4. (a) Total, discharge, and capacitive energy for the jet without and with the different targets at a distance of 1 cm. Solid markers indicate not grounded targets and open markers indicate grounded targets. "No" means that no target is present. (b) Electric field in a freely expanding jet as a function of distance from the anode, measured at two different helium lines.

two electric field values would be present at the same position on the x-axis.

It should be noted that after the end of the measurements, the plasma plume still continues over a few centimeters, but the light intensity is too low to obtain spectra and hence no electric field can be calculated. The results of the two lines show good resemblance, giving confidence on the obtained values. For the 447.1 nm line, the error bars are larger because of lower emission intensity. The electric field between the anode and the cathode is highest, since here the plasma is created and no plasma bullets are formed yet. From the cathode until the end of the capillary, the electric field slightly decreases, because the ionization wave moves away from the plasma source, losing energy and charge on its way. For the same configuration but powered with AC voltage, the charging of the wall of the capillary was estimated to be 7.5 pC/mm.[26] When the ionization wave enters the surrounding air, the electric field increases, corresponding to the results for an AC powered jet[3] and for a pulsed plasma jet.[29] Out of the capillary, the helium plasma mixes with oxygen and nitrogen gas from the air, leading to a contraction of the ionization front, hence the charges are confined in a smaller volume which yields a higher electric field. For the same AC powered jet, the slopes of the electric field both inside and outside the capillary as shown by Sretenović *et al.*[30] with the same flow of 1.5 slm are the same as the results shown here, only with a higher offset value in this work. This shows that the flow is the main driving parameter of the electric field enhancement in the plasma plume, as in the setup of Sretenović *et al.*[30] the driving voltage has a different shape (both in frequency and in amplitude).

In Figs. 5 and 6, the influence of a target on the electric field is shown. Figure 5 shows the results of the different targets, placed at a distance of 1 cm from the capillary and at a floating potential (not grounded). It can be seen that the electric field for the plastic, insulating target is almost the same as if there would be no target. From the electric field in the plasma plume it has already been shown that gas mixing influences the plasma.[3] Placing an insulating target close to the capillary shortens the path of the plasma plume, but since this has no effect on the electric field, it can be concluded that the gas mixing does not play a role in this particular configuration, probably because a high flow (1.5 slm) is applied. This keeps the helium flow pure all the way to the target, which Ries *et al.*[31] observed by LIF measurements of a plasma jet impinging on a metal and on a water target.

Distilled water, saline, chicken breast, and copper all show a higher electric field, with an almost constant value in the gap between the capillary and the target. The dependence of the electric field on the dielectric constant and on the conductivity of the target is shown, respectively, in Figs. 7(a) and 7(b), where the field is measured at 2 mm outside the capillary and the not grounded targets are placed 1 cm from the capillary. Values for the dielectric constant are taken from the literature[32–34] and values for the electrical conductivity likewise.[35–37] For chicken, the actual value for these constants can differ from the values presented here, since the composition can easily differ between one piece and another. The electric field increases with increasing dielectric constant and reaches a somewhat constant value of 20 kV/cm at $\epsilon \approx 70$. This trend was also found by modeling.[38] An increase in the conductivity also leads to an increase in the electric field. Even more, the energy measurements [Fig. 4(a)] are consistent with the electric field measurements for the different targets.

When the plasma bullet hits the target, two different behaviors are observed, equal to what is shown by Klarenaar *et al.*[39] with the same jet setup and for a dielectric (glass), distilled water, and copper target. For targets with a low dielectric constant or conductivity, the arrival of the plasma

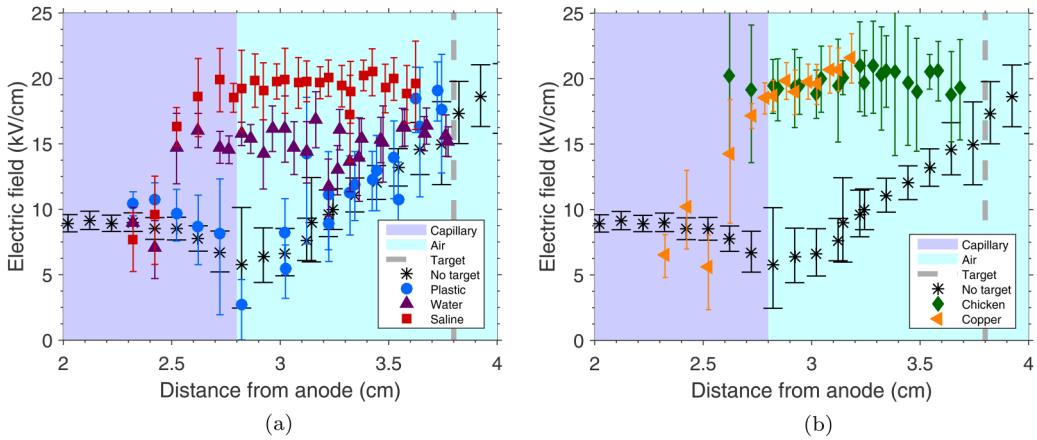

FIG. 5. Electric field as a function of distance from the anode for different non-grounded targets at 1 cm from the capillary: (a) plastic (PVC), distilled water and saline (19 g/l), and (b) chicken breast and copper.

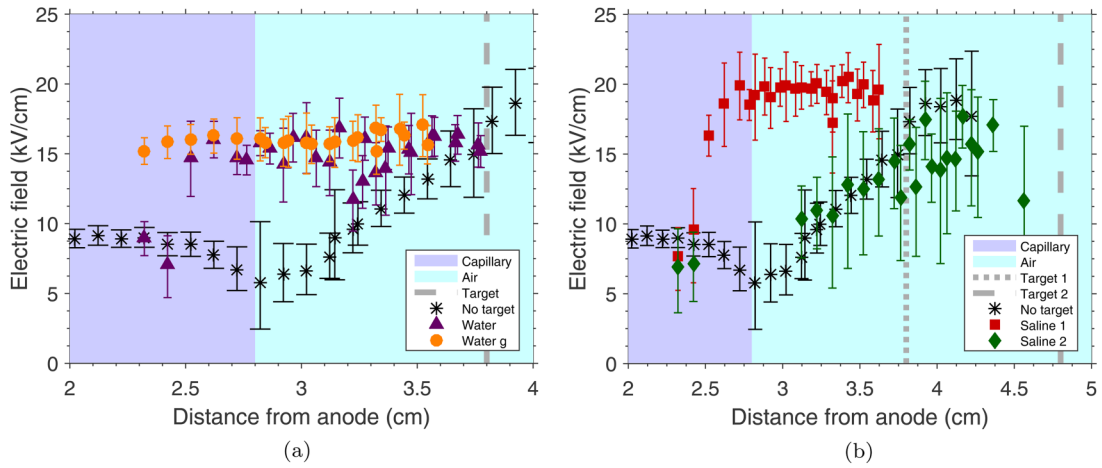

FIG. 6. Electric field as a function of distance from the anode for (a) a non-grounded and a grounded distilled water target at 1 cm from the capillary and (b) a non-grounded saline target at a distance of 1 cm and 2 cm from the capillary. Note the different *x*-axis in (b).

bullet on the target leads to charging of the surface, inducing surface ionization waves that propagate over the target surface, which was also predicted by modeling.[40] These surface ionization waves then lead to a radial electric field along the target surface. For targets with a high dielectric constant or conductivity, no surface ionization waves are observed, but instead, after hitting the target, a return stroke of the plasma bullet occurs which travels back into the plasma channel and the capillary. This return stroke (also called restrike, reversed bullet or rebound) for helium plasmas at atmospheric pressure was predicted by modeling for a plasma jet impinging on a metal substrate[41–43] and was also seen experimentally with a needle-to-plane discharge,[44] with a plasma jet impinging on different conductive targets (e.g., mouse skin and metallic plate)[31] and with a plasma jet impinging on a grounded metallic target.[45] By measuring the electric field with an electro-optic probe at the outside of the plasma jet capillary, Darny *et al.*[45] have shown that the electric field of the rebounding front is lower than the initial front. The return stroke appears less than 10 ns after the first impact of the plasma on the target.[39] Although we have a long exposure time of 200 ns, we do not measure the contribution of this second front to the electric field. Therefore, the two fronts are either at the same position in the spectrum, or the

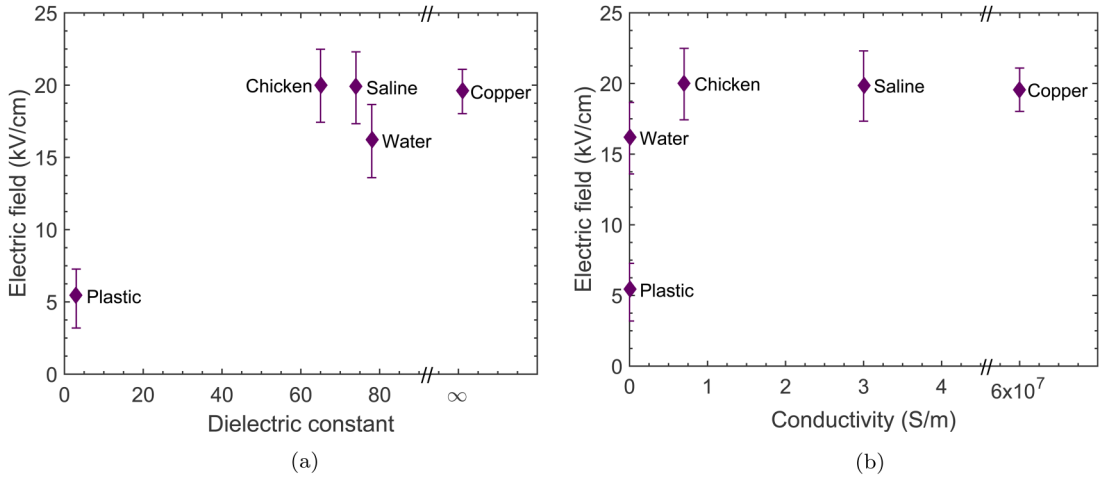

FIG. 7. Electric field as a function of (a) the dielectric constant and (b) the conductivity of the target, measured 2 mm outside the capillary with a target placed at 1 cm from the capillary.

second one has a too low intensity or field to detect. Thus, the measured electric field is only of the first ionization front. This means that the increase in the electric field for targets with a higher dielectric constant cannot be explained by the additional contribution of the second ionization front.

As such, it is not yet fully understood why the electric field is higher for a target with a higher dielectric constant or conductivity, even before the bullet hits the target. It suggests a long lasting effect that influences the bullet propagation from one pulse to the next one. A possible explanation can be found in the work of McKay *et al.*[46] Here, mass spectroscopy is performed on an atmospheric pressure helium jet with similar dimensions to study the ionic composition of the jet. It was found that, at an applied voltage similar to this work (4 kV pulses at 5 kHz), negative ions have a long residence time in between the pulses. This could imply that there are still negative ions present in the gap from the previous plasma ionization front when the next front arrives, influencing the propagation, charge separation, and thus electric field in the head of this front. Also, the return stroke is present every time the electric field has a flat profile. Having this flat profile means that the electric field is high all the way from the capillary to the target, which would make it easier for the return stroke to exist and to propagate. Although this might be the reason why the return stroke occurs, the reason why the electric field has such a flat profile still remains unknown.

The influence of grounding the target is shown in Fig. 6(a) for the distilled water target. Within the error-bars, the electric field is the same, but the value is more constant and the error-bars are smaller for the grounded target, since the light intensity is higher. A similar behavior of the electric field inside the capillary was observed by Sretenović *et al.* for an AC powered atmospheric pressure plasma jet in helium with a grounded electrode at 1 cm from the end of the capillary. A constant electric field at a value of about 20 kV/cm was obtained over the length of the capillary after the powered electrode,[25] which is in good comparison with the results shown here.

Changing the distance between the capillary and the target leads to the results shown in Fig. 6(b) for the saline target. With a target at 2 cm, the electric field is lower than that with a target at 1 cm and it is almost the same as if there would be no target. The voltage difference between the anode and the target is smaller at a larger distance and at 2 cm it is too small to have an influence on the electric field, and thus the electric field is almost the same as without a target.

IV. CONCLUSIONS

In this paper, electric field measurements of a kHz pulsed helium jet both without and with the presence of a target are reported. The trend of the electric field of the jet without interacting with a target corresponds to results in the literature.[3,29,30] It was found that placing a target in front of the jet has a strong influence on the plasma. A relation exists between the dielectric constant or the conductivity of the target and the electric field: a higher dielectric constant or conductivity yields a higher electric field. This relation corresponds to results found by modeling.[38] For conductive targets, a return stroke of the plasma bullet was observed that propagates from the target into the direction of the capillary, after the plasma bullet has hit the target.[39] However, the return stroke does not contribute to the measured electric field and, as such, it cannot explain the increase in the electric field for targets with an increasing dielectric constant or conductivity.

Grounding of the targets was found to have a negligible effect on the amplitude of the electric field, but it shows a more constant behavior and the error-bars are smaller. An increase in the distance between the capillary and the target was shown to yield lower electric field values and, especially for non-grounded targets, an overall behavior that is more similar to the results without a target.

APPENDIX A: THEORETICAL CALCULATION

1. Derivation

To be able to calculate the electric field from the spectra that will be measured, it is necessary to know the energy levels of helium in an external electric field. Therefore, the time-independent Schrödinger equation needs to be solved

$$H\psi = E\psi. \tag{A1}$$

For the hydrogen atom, with hamiltonian

$$H_H = -\frac{\hbar^2}{2m}\nabla^2 - \frac{e^2}{4\pi\epsilon_0}\frac{1}{r}, \tag{A2}$$

exact solutions to the Schrödinger equation can be found by using spherical coordinates and separation of variables

$$\psi(r, \theta, \phi) = R(r)Y(\theta, \phi). \tag{A3}$$

Elaborated calculations can be found in the literature,[24,47–49] and here, only the results will be given. The radial wave function is given by

$$R_{nl}(r) = \sqrt{\left(\frac{2}{na_0}\right)^3 \frac{(n-l-1)!}{2n[(n+l)!]^3}}\, e^{-r/na_0} \left(\frac{2r}{na_0}\right)^l \left[L^{2l+1}_{n-l-1}(2r/na_0)\right], \tag{A4}$$

where a_0 is the Bohr radius and $L^p_{q-p}(x)$ is an associated Laguerre polynomial, given by

$$L^p_{q-p}(x) = (-1)^p \left(\frac{d}{dx}\right)^p L_q(x) \tag{A5}$$

and L_q is the qth Laguerre polynomial

$$L_q(x) = e^x \left(\frac{d}{dx}\right)^q (e^{-x}x^q). \tag{A6}$$

The angular wave function is given by

$$Y_l^m(\theta, \phi) = \epsilon \sqrt{\frac{2l+1}{4\pi}\frac{(l-|m|)!}{(l+|m|)!}} P_l^m(\cos\theta) e^{im\phi}, \tag{A7}$$

in which $\epsilon = (-1)^m$ for $m \geq 0$ and $\epsilon = 1$ for $m \leq 0$. P_l^m is the associated Legendre function, defined by

$$P_l^m(x) = (1-x^2)^{|m|/2} \left(\frac{d}{dx}\right)^{|m|} P_l(x) \tag{A8}$$

and $P_l(x)$ is the lth Legendre polynomial, defined by the Rodrigues formula

$$P_l(x) = \frac{1}{2^l l!} \left(\frac{d}{dx}\right)^l (x^2-1)^l. \tag{A9}$$

The total wave function is then found by substituting Eqs. (A4) and (A7) back into Eq. (A3).

For the helium atom, however, these exact solutions do not exist, but it will be shown that the solutions for the hydrogen atom can also be used for the helium atom. The hamiltonian of the helium atom is given by

$$H_{He} = -\frac{\hbar^2}{2m}\nabla_1{}^2 - \frac{e^2}{2\pi\epsilon_0}\frac{1}{r_1} - \frac{\hbar^2}{2m}\nabla_2{}^2 - \frac{e^2}{2\pi\epsilon_0}\frac{1}{r_2} + \frac{e^2}{2\pi\epsilon_0}\frac{1}{r_{12}}, \tag{A10}$$

where r_1 and r_2 give the distance from the nucleus to electrons 1 and 2, and r_{12} gives the mutual distance between the two electrons. The first two terms correspond to one electron of the atom, the second two terms to the other electron, and the last term to the interaction between the two electrons. One electron occupies the ground state and the other electron occupies an excited state. When the excited level is a low-lying level, the wave functions of the two electrons overlap and thus they can influence one another. Here, the two electrons are considered to be far enough apart to not influence one another. The validation of this approximation is found by looking at the Coulomb force[50]

$$F_e = \frac{e^2}{4\pi\epsilon_0}\frac{1}{r_{12}^2}, \tag{A11}$$

where the distance between the two electrons, r_{12}, will be linked to the radius of the electron orbital, given by[51]

$$a_n = \frac{a_0 n^2}{Z}, \tag{A12}$$

in which a_0 is the Bohr radius. For the case when both electrons are in the ground state ($n = 1$), the maximum distance between the two electrons is twice the radius of the first electron orbital:

$$r_{12} = 2a_1 = a_0.$$

In the case considered here, one electron is in the first electron orbital and one electron in the fourth electron orbital ($n = 4$). The minimum distance between these two electrons is

$$r_{12} = a_4 - a_1 = \frac{15a_0}{2}.$$

Thus, the distance between the electrons in this case is at least a factor 15/2 larger than the distance between two electrons in the ground state. Regarding Eq. (A11), this yields a Coulomb force of at least $(15/2)^2$ times smaller, validating the approximation that wave functions of the two electrons in our case are not overlapping.

Another argument is found by looking at the exchange integral J_{ex}, which is a measure for the frequency with which the two electrons exchange their quantum states, given by[48]

$$J_{ex} = \frac{4Z^3(Z-1)^{2n+1}n^2}{[Z(n+1)-1]^{2n+3}}\frac{2n+3}{2n-1}. \tag{A13}$$

After time interval $\pi/2J_{ex}$, the two electrons have interchanged their respective roles, and after time interval π/J_{ex}, they are back in their original orbits. Here, time is measured in the atomic unit $1/4\pi$Ry, where Ry is the Rydberg frequency. The period of exchange τ (in cgs units) is then given by

$$\tau = \frac{\pi}{J_{ex}}\frac{1}{4\pi Ry} = \frac{1}{4J_{ex}Ry} = \frac{0.75\cdot 10^{-16}\,s}{J_{ex}}. \tag{A14}$$

The transitions of the helium atom used in this study take place at $n = 4$ and helium has $Z = 2$, yielding $J_{ex} = 2.56\cdot 10^{-8}$ and $\tau = 17.56$ s. The residence time of the helium atoms in the plasma jet in this study is much smaller, in the order of μs to ns, thus the exchange period of the electrons is long enough to have no overlap in their wave functions.

Therefore, the interaction term in the hamiltonian can be neglected and what is left is the hamiltonian of the hydrogen atom with an extra charge.

Placing the atom in an externally applied electric field leads to a perturbation of the hamiltonian, because of the interaction between the electron of the atom and the electric

field, given by

$$H^{1'} = eFz, \tag{A15}$$

where the applied field $F = |\vec{E}|$ is directed along the positive z-axis. To account for the extra charge in the nucleus of the helium atom, compared to the hydrogen atom, an extra entry is added to the perturbed hamiltonian, which corresponds to the difference in energy between the hydrogen and helium terms with the same n, as a function of l

$$H^{1''} = hc\nu_l, \tag{A16}$$

in which ν_l is the difference (in cm^{-1}) between the helium and the corresponding hydrogen terms. The total perturbation to the hamiltonian [Eq. (A2)] is then

$$H^1 = H^{1'} + H^{1''} = eFz + hc\nu_l. \tag{A17}$$

To solve the Schrödinger equation with this addition, perturbation theory needs to be applied. Since the solution of the unperturbed Schrödinger equation leads to degenerate energy levels, the non-degenerate perturbation theory is not valid and thus degenerate perturbation theory has to be applied.

When the energy E_n^0 is g_n-fold degenerate, there are g_n wave functions with the same energy E_n^0. The unperturbed Schrödinger equation

$$H^0\psi_n^0 = E_n^0\psi_n^0 \tag{A18}$$

then changes into

$$H^0\psi_{ni}^0 = E_n^0\psi_{ni}^0, \quad i = 1, 2, \ldots, g_n, \tag{A19}$$

where H^0 is given by Eq. (A2). The degenerate wave functions can be written as a linear combination

$$\psi_n^0 = \sum_{i=1}^{g_n} c_{ni}\psi_{ni}^0, \tag{A20}$$

which is too an eigenfunction of the unperturbed hamiltonian, with the same eigenvalue

$$\begin{aligned} H^0\psi_n^0 = \sum_{i=1}^{g_n} c_{ni}H^0\psi_{ni}^0 = E_n^0\sum_{i=1}^{g_n} c_{ni}\psi_{ni}^0 \\ = E_n^0\psi_n^0. \end{aligned} \tag{A21}$$

Still, the Schrödinger equation [Eq. (A1)] needs to be solved, which changes into

$$(H^0 + H^1)\psi_{ni} = E_{ni}\psi_{ni}, \quad i = 1, 2, \ldots, g_n. \tag{A22}$$

Because H^1 is a small perturbation, the eigenvalues and eigenfunctions can be written as expansion series

$$E_{ni} = E_n^0 + E_{ni}^1 + E_{ni}^2 + \cdots, \quad i = 1, 2, \cdots, g_n, \tag{A23}$$

$$\psi_{ni} = \psi_{ni}^0 + \psi_{ni}^1 + \psi_{ni}^2 + \cdots, \quad i = 1, 2, \cdots, g_n, \tag{A24}$$

where E_n^0 is the same for all values of i. Substituting these expressions into Eq. (A22) gives, up to first order,

$$H^0\psi_{ni}^0 = E_n^0\psi_{ni}^0, \tag{A25}$$

$$H^0\psi_{ni}^1 + H^1\psi_{ni}^0 = E_n^0\psi_{ni}^1 + E_{ni}^1\psi_{ni}^0, \tag{A26}$$

where Eq. (A25) is just the unperturbed Schrödinger equation [Eq. (A18)]. The first order correction will now be calculated, and analogously higher order corrections can be calculated. Taking the inner product of ψ_{ni}^0 with Eq. (A26) gives

$$\begin{aligned} \langle\psi_{ni}^0|H^0\psi_{ni}^1\rangle + \langle\psi_{ni}^0|H^1\psi_{ni}^0\rangle = E_n^0\langle\psi_{ni}^0|\psi_{ni}^1\rangle \\ + E_{ni}^1\langle\psi_{ni}^0|\psi_{ni}^0\rangle. \end{aligned} \tag{A27}$$

The hermitian property of H^0 makes the first term on the left and right hand side cancel against one another, leaving

$$\langle\psi_{ni}^0|H^1\psi_{ni}^0\rangle = E_{ni}^1\langle\psi_{ni}^0|\psi_{ni}^0\rangle. \tag{A28}$$

Substituting Eq. (A20) and using the orthonormality $\langle\psi_{ki}^0|\psi_{ni}^0\rangle = \delta_{kn}$ yields

$$\begin{aligned} \sum_{j=1}^{g_n} c_{nj}\langle\psi_{ni}^0|H^1|\psi_{nj}^0\rangle = E_{ni}^1\sum_{j=1}^{g_n} c_{nj}\langle\psi_{ni}^0|\psi_{nj}^0\rangle \\ = E_{ni}^1 c_{ni} \end{aligned} \tag{A29}$$

or

$$\sum_{j=1}^{g_n} c_{nj}\left(H_{ni,nj}^1 - E_{ni}^1\delta_{ij}\right) = 0, \tag{A30}$$

where $H_{ni,nj}^1 = \langle\psi_{ni}^0|H^1|\psi_{nj}^0\rangle$. For Eq. (A30), a trivial solution is $c_{nj} = 0$ for all j. A non-trivial solution only exists if the determinant with elements $(H_{ni,nj}^1 - E_{ni}^1\delta_{ij})$ vanishes, which yields the secular equation

$$|H_{ni,nj}^1 - E_{ni}^1\delta_{ij}| = 0. \tag{A31}$$

Satisfied, it will give g_n roots: $E_{n1}^1, E_{n2}^1, \ldots, E_{ng_n}^1$, yielding the

first-order corrections to the degenerate eigenvalues

$$E_{ni} = E_n^0 + E_{ni}^1, \quad i = 1, 2, \ldots, g_n. \tag{A32}$$

Because of the perturbation, the degeneracy is removed as it vanishes. Instead, the degenerate level E_n is split into sub-levels with energies given in Eq. (A32) and the appropriate wave functions ψ_{ni}.

Returning to the case of the helium atom in an external electric field, the energy levels E_n (principal quantum number n) split into m (magnetic quantum number) sub-levels, in which the individual terms are arranged to index l (angular momentum quantum number). Since only linearly polarized light is taken into account, $\Delta m = 0$ and thus $m = m'$. The secular equation [Eq. (A31)]), which needs to be solved, becomes then

$$\left| H^1_{nlm,nl'm} - E^1 \delta_{ll'} \right| = 0, \quad |m| \le l \le (n-1), \tag{A33}$$

where the matrix elements $H^1_{nlm,nl'm}$ are given by the inner product of Eq. (A17) with the unperturbed eigenfunctions $\psi_{nlm}(r, \theta, \phi)$. Then, Eq. (A33) gives

$$\begin{vmatrix} H_{ll} - E^1 & H_{l,l+1} & \ldots & H_{l,n-1} \\ H_{l+1,l} & H_{l+1,l+1} - E^1 & \ldots & H_{l+1,n-1} \\ \ldots & \ldots & \ldots & \ldots \\ H_{n-1,l} & H_{n-1,l+1} & \ldots & H_{n-1,n-1} - E^1 \end{vmatrix} = 0. \tag{A34}$$

The quantum numbers n and m are still inside Eq. (A34), but since they are constant for every element in the matrix, they are not written for simplicity. The matrix elements $H_{ll'}$ are given by

$$\begin{aligned} H_{ll'} &= eF \int \psi_{nlm}(\vec{r}) z \psi^*_{nl'm}(\vec{r})\, d\vec{r} \\ &\quad + hc\nu_l \int \psi_{nlm}(\vec{r}) \psi^*_{nl'm}(\vec{r})\, d\vec{r}. \end{aligned} \tag{A35}$$

The second integral yields $hc\nu_l\delta_{ll'}$, while using spherical coordinates ($z = r\cos\theta$) and Eq. (A3), the first integral becomes

$$eF \int_0^\infty R_{nl} r R_{nl'} r^2\, dr \int_0^{4\pi} Y_{lm} \cos\theta Y^*_{l'm}\, d\Omega.$$

The radial wave function is given by Eq. (A4), yielding[24,48]

$$\begin{aligned} \int_0^\infty R_{nl-1} r R_{nl}\, r^2\, dr &= \int_0^\infty R_{nl} r R_{nl-1} r^2\, dr \\ &= \frac{3}{2} a_0 n \sqrt{n^2 - l^2} \end{aligned} \tag{A36}$$

and the angular wave function is given by Eq. (A7), yielding[24,48]

$$\begin{aligned} \int_0^{4\pi} Y_{l-1m} \cos\theta Y^*_{lm}\, d\Omega &= \int_0^{4\pi} Y_{lm} \cos\theta Y^*_{l-1m}\, d\Omega \\ &= \sqrt{\frac{l^2 - m^2}{(2l+1)(2l-1)}}. \end{aligned} \tag{A37}$$

Thus, the first term of Eq. (A35) is given by

$$\begin{aligned} H_{l-1,l} &= H_{l,l-1} \\ &= \frac{3}{2} eF a_0 n \sqrt{n^2 - l^2} \sqrt{\frac{l^2 - m^2}{(4l^2 - 1)}}, \end{aligned} \tag{A38}$$

which are off-diagonal elements, while the second term is given by

$$H_{ll'} = hc\nu_l \delta_{ll'}, \tag{A39}$$

which are diagonal elements. Dividing all elements by −1 and setting

$$f(n, m, l) = f_{nml} = \frac{(n^2 - l^2)(l^2 - m^2)}{(4l^2 - 1)} \tag{A40}$$

and

$$\kappa = \frac{3ea_0}{2hc} \approx 6.40 \cdot 10^{-5}\ \mathrm{cm}^{-1}, \tag{A41}$$

gives the secular equation for the helium atom

$$\begin{bmatrix} \nu_l + E^1 & -n\kappa F\sqrt{f_{nml+1}} & 0 & \ldots \\ -n\kappa F\sqrt{f_{nml+1}} & \nu_{l+1} + E^1 & -n\kappa F\sqrt{f_{nml+2}} & \ldots \\ 0 & -n\kappa F\sqrt{f_{nml+2}} & \nu_{l+2} + E^1 & \ldots \\ \ldots & \ldots & \ldots & \ldots \end{bmatrix} = 0. \tag{A42}$$

The displacements of the energy levels are measured from the diffuse (D) line, therefore, $x = E^1 + \nu_l$, which is the displacement of the helium line in cm^{-1}, measured from the D-line and $\lambda_l = \nu_2 - \nu_l$ are substituted into the previous matrix to yield the final secular equation

$$\begin{vmatrix} x + \lambda_l & -n\kappa F\sqrt{f_{nml+1}} & 0 & \ldots \\ -n\kappa F\sqrt{f_{nml+1}} & x + \lambda_{l+1} & -n\kappa F\sqrt{f_{nml+2}} & \ldots \\ 0 & -n\kappa F\sqrt{f_{nml+2}} & x + \lambda_{l+2} & \ldots \\ \ldots & \ldots & \ldots & \ldots \end{vmatrix} = 0. \tag{A43}$$

In this study, two helium lines are considered. The secular equation will be solved for both lines, yielding expressions for the wavelength shift as a function of the electric field.

The allowed transition at the 492.2 nm helium line is $1s4d\,^1D \rightarrow 1s2p\,^1P^o$ and the forbidden transition is $1s4f\,^1F^o \rightarrow 1s2p\,^1P^o$. Therefore, we have the line groups $4(S, P, D, F) \rightarrow 2P$, or $n = 4(l = 0, 1, 2, 3) \rightarrow n = 2(l = 1)$, at $S = 0$. For $m = 1$, $|m| \le l \le (n-1) \leftrightarrow 1 \le l \le 3$ and the matrix in Eq. (A43) is a 3×3 matrix, thus the equation we need to solve is

$$\begin{vmatrix} x+\lambda_1 & -4\kappa F\sqrt{f(4,1,2)} & 0 \\ -4\kappa F\sqrt{f(4,1,2)} & x & -4\kappa F\sqrt{f(4,1,3)} \\ 0 & -4\kappa F\sqrt{f(4,1,3)} & x+\lambda_3 \end{vmatrix} = 0.$$

From the data in Tables I and II, λ_1 and λ_3 have been calculated to give $\lambda_1 = 46.3\,\mathrm{cm}^{-1}$ and $\lambda_3 = 5.43\,\mathrm{cm}^{-1}$. Furthermore, we have

$$f(4,1,2) = \frac{12}{5}, \quad f(4,1,3) = \frac{8}{5}$$

to get

$$\begin{vmatrix} x+\lambda_1 & -4\kappa F\sqrt{\frac{12}{5}} & 0 \\ -4\kappa F\sqrt{\frac{12}{5}} & x & -n\kappa F\sqrt{\frac{8}{5}} \\ 0 & -n\kappa F\sqrt{\frac{8}{5}} & x+\lambda_3 \end{vmatrix} = 0.$$

Expanded, this gives the characteristic polynomial equation

$$\begin{aligned} &x^3 + x^2(\lambda_1+\lambda_3) + x\left[\lambda_1\lambda_3 - 4(4\kappa F)^2\right] \\ &- (4\kappa F)^2\left(\frac{8}{5}\lambda_1 + \frac{12}{5}\lambda_3\right) = 0, \end{aligned} \tag{A44}$$

which has three solutions, for the energy levels $l = 1, 2, 3 \leftrightarrow P, D, F$.

For the $n = 4$, $m = 0$, $S = 0$ level, $|m| \le l \le (n-1) \leftrightarrow 0 \le l \le 3$ and the matrix in Eq. (A43) is a 4×4 matrix, thus the secular equation becomes

$$\begin{vmatrix} x+\lambda_0 & -4\kappa F\sqrt{5} & 0 & 0 \\ -4\kappa F\sqrt{5} & x+\lambda_1 & -4\kappa F\sqrt{\frac{16}{5}} & 0 \\ 0 & -4\kappa F\sqrt{\frac{16}{5}} & x & -4\kappa F\sqrt{\frac{9}{5}} \\ 0 & 0 & -4\kappa F\sqrt{\frac{9}{5}} & x+\lambda_3 \end{vmatrix} = 0,$$

where

$$f(4,0,1) = 5, \quad f(4,0,2) = \frac{16}{5}, \quad f(4,0,3) = \frac{9}{5}$$

have already been substituted and $\lambda_0 = -506.2\,\mathrm{cm}^{-1}$. The characteristic polynomial equation is

$$\begin{aligned} &x^4 + x^3(\lambda_0+\lambda_1+\lambda_3) \\ &+ x^2\left[\lambda_0\lambda_1 + \lambda_1\lambda_3 + \lambda_0\lambda_3 - 10(4\kappa F)^2\right] \\ &+ x\left[\lambda_0\lambda_1\lambda_3 - (4\kappa F)^2\left(5\lambda_0 + \frac{9}{5}\lambda_1 + \frac{41}{5}\lambda_3\right)\right] \\ &- (4\kappa F)^2\lambda_0\left(\frac{9}{5}\lambda_1 + \frac{16}{5}\lambda_3\right) \\ &+ 9(4\kappa F)^4 = 0. \end{aligned} \tag{A45}$$

For the $n = 4$, $m = 2$, $S = 0$ level, $|m| \le l \le (n-1) \leftrightarrow 2 \le l \le 3$ and the matrix in Eq. (A43) is a 2×2 matrix, thus the secular equation becomes

$$\begin{vmatrix} x & -4\kappa F \\ -4\kappa F & x+\lambda_3 \end{vmatrix} = 0,$$

where

$$f(4,2,1) = 1$$

has already been substituted and the characteristic polynomial is

$$x^2 + \lambda_3 x - (4\kappa F)^2 = 0. \tag{A46}$$

TABLE I. Energy levels of helium I.[52]

S	n	L	J	Conf.	Term symbol	Energy (cm^{-1})
0	4	0	0	1s4s	^1S	190 940.226355
0	4	1	1	1s4p	$^1P^0$	191 492.711909
0	4	2	2	1s4d	^1D	191 446.4557405
0	4	3	3	1s4f	$^1F^0$	191 451.89746084
1	4	0	1	1s4s	^3S	190 298.113260
1	4	1	2	1s4p	$^3P^0$	191 217.040967
1	4	2	3	1s4d	^3D	191 444.4809292
1	4	3	4	1s4f	$^3F^0$	191 451.88108855

TABLE II. Energy levels of hydrogen I.[53]

S	n	L	J	Conf.	Term symbol	Energy (cm^{-1})
−1/2	4	0	1/2	4s	^2S	102 823.8530211
−1/2	4	1	1/2	4p	$^2P^0$	102 823.8485825
−1/2	4	2	3/2	4d	^2D	102 823.894250
−1/2	4	3	5/2	4f	$^2F^0$	102 823.909490
1/2	4	0	1/2	4s	^2S	102 823.8530211
1/2	4	1	3/2	4p	$^2P^0$	102 823.8943175
1/2	4	2	5/2	4d	^2D	102 823.9094871
1/2	4	3	7/2	4f	$^2F^0$	102 823.917091

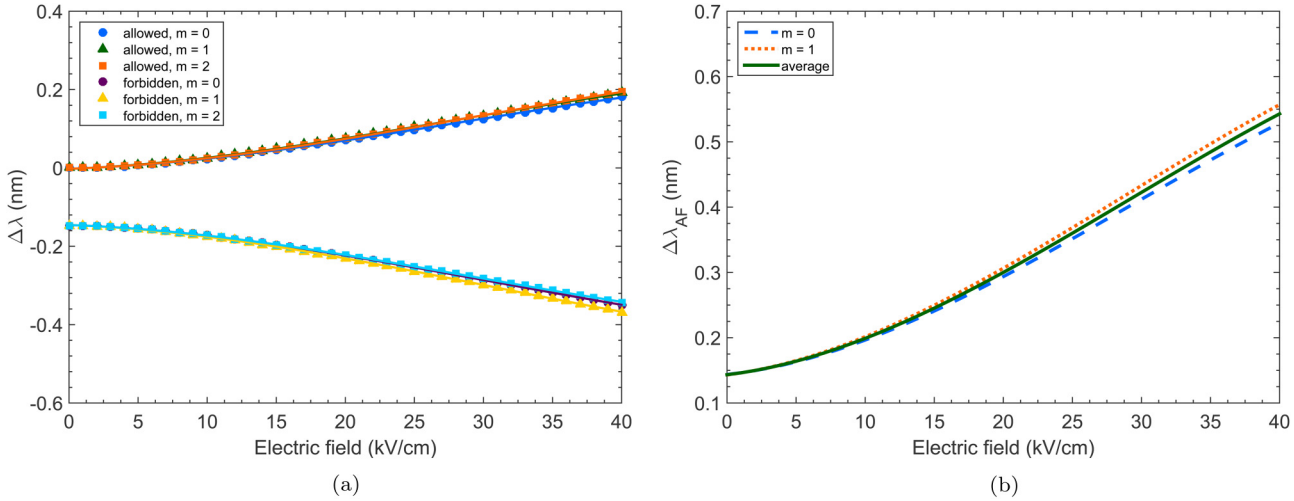

FIG. 8. Results of the theoretical calculation for the He I 447.1 nm line: (a) the shift in wavelength of the forbidden and the allowed line as a function of the electric field and (b) the difference between the shifted allowed and forbidden line as a function of the electric field.

The allowed transition at the 447.1 nm helium line is $1s4d\,^3D \rightarrow 1s2p\,^3P^o$ and the forbidden transition is $1s4f\,^3F^o \rightarrow 1s2p\,^3P^o$. Compared to the transitions at the helium 492.2 nm line, the only quantum number that changes is the total spin S. Because this only influences the energy levels and thus the values of the λ_i, the calculation and thus the characteristic polynomial equations are equal for the 447.1 nm line and only the λ_i need to be adapted. λ_0, λ_1, and λ_3 are again calculated from the data in Tables I and II to give $\lambda_0 = -1146.3\,\mathrm{cm}^{-1}$, $\lambda_1 = -227.42\,\mathrm{cm}^{-1}$, and $\lambda_3 = 7.39\,\mathrm{cm}^{-1}$.

The results for the displacement as a function of the electric field for both the allowed transition (L = 2) and the forbidden transition (L = 3) for different values of $m(0, 1, 2)$ are shown as the symbols in Figs. 8(a) and 9(a). Third order polynomials have been fitted to the curves. These fitted curves are also shown in Figs. 8(a) and 9(a) as the lines through the data points. As explained in Appendix B and by using a linear polarizer, since the axial field is measured, only the π-components ($\Delta m = 0$) are detected. Therefore, the polynoms of only the $m_i = 0 \rightarrow m_k = 0$ and $m_i = 1 \rightarrow m_k = 1$

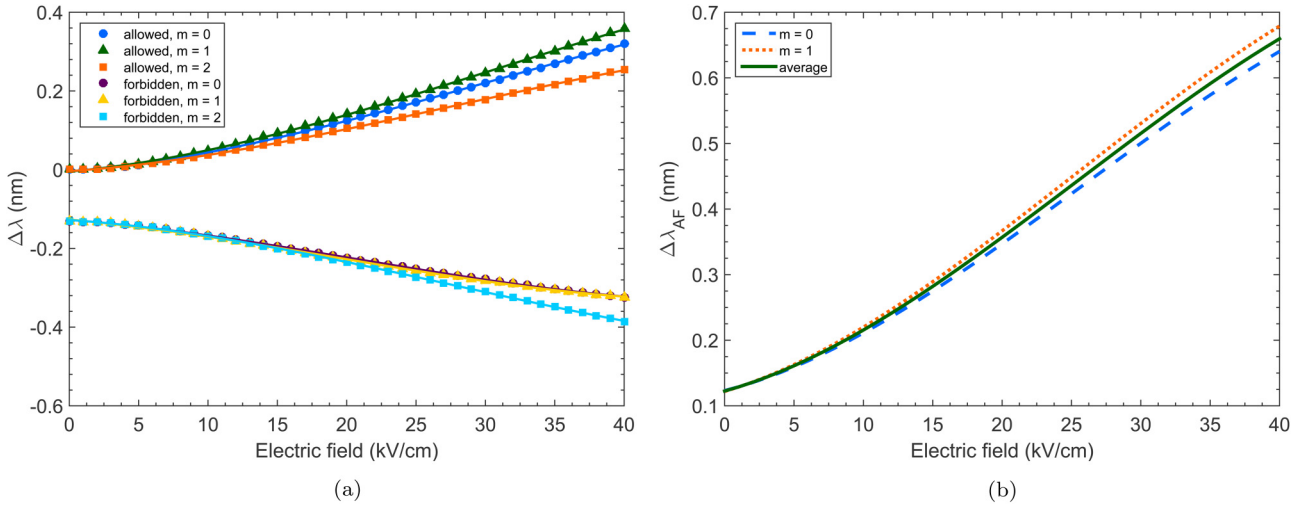

FIG. 9. Results of the theoretical calculation for the He I 492.2 nm line: (a) the shift in wavelength of the forbidden and the allowed line as a function of the electric field and (b) the difference between the shifted allowed and forbidden line as a function of the electric field.

components are used to calculate the difference between the allowed and the forbidden band, and not the transitions with $\Delta m = \pm 1$. These curves are shown in Figs. 8(b) and 9(b), together with the average of these two components. The curves in Figs. 8(a) and 9(a) for the forbidden and the allowed components are so close together that the different m components cannot be resolved with the used setup. Instead, only one allowed and forbidden band can be detected. Therefore, the curves of the $m = 0$ and $m = 1$ components are averaged to obtain a single relation between the difference of the allowed and forbidden band, and the electric field. This average curve will be used to calculate the electric field from the difference between the allowed and the forbidden peak of the lines that will be measured in the experiments. For He I 492.2 nm, it is given by

$$\Delta\lambda_{AF} = -5.2140 \cdot 10^{-6}E^3 + 3.9844 \cdot 10^{-4}E^2 + 0.0058E + 0.1226, \quad \text{(A47)}$$

with $\Delta\lambda_{AF}$ in nm and E in kV/cm, and for He I 447.1 nm it is

$$\Delta\lambda_{AF} = -3.9620 \cdot 10^{-6}E^3 + 3.4558 \cdot 10^{-4}E^2 + 0.0025E + 0.1433. \quad \text{(A48)}$$

The electric field in the experiment is obtained by numerically solving the above equations for E with the measured wavelength difference substituted for $\Delta\lambda_{AF}$.

2. Comparison to previous work

In this paragraph, the resulting relation between $\Delta\lambda_{AF}$ and the electric field is compared to the relation obtained from Cvetanovic *et al.*,[8] Foster,[20] and Kuraica.[24]

The supplementary material of Cvetanovic *et al.* gives the wavelength shift of the different $n = 4$ levels for the He I 447.1 nm line and the He I 492.2 nm line, as a function of the electric field (ranging from 0 kV/cm to 101 kV/cm, in steps of 1 kV/cm). From these shifts, the distance between the shifted allowed and forbidden components is calculated as a function of the electric field. Similar to Figs. 8(b) and 9(b), the average is taken over the $\Delta m = 0$ components with $m = m' = 0, 1$, to obtain the relation $\Delta\lambda_{AF}(E)$ for the two helium lines.

Foster gives the energy shift of the different $n = 4$ levels for the He I 447.1 nm line and the He I 492.2 nm line for electric fields from 0 kV/cm to 100 kV/cm, in steps of 10 kV/cm. These energy shifts are first converted to wavelength shifts and then the same procedure is followed as with the results from Cvetanovic *et al.*

From Kuraica, the relations $\Delta\lambda_{AF}(E)$ are directly taken for the He I 447.1 nm line and the He I 492.2 nm line. It is important to note that this relation is only valid from 0 kV/cm to 20 kV/cm.[24]

The results from these calculations together with the results from this paper are shown in Fig. 10 for the two helium lines. In the bottom graphs, the deviation of the different results to this paper is shown.

For the results of Foster, the data are only given in steps of 10 kV/cm, and since only partly data were given at 0 kV/cm, no data point is possible there. At electric fields below 20 kV/cm, the deviation in the results is with up to 10%–15%

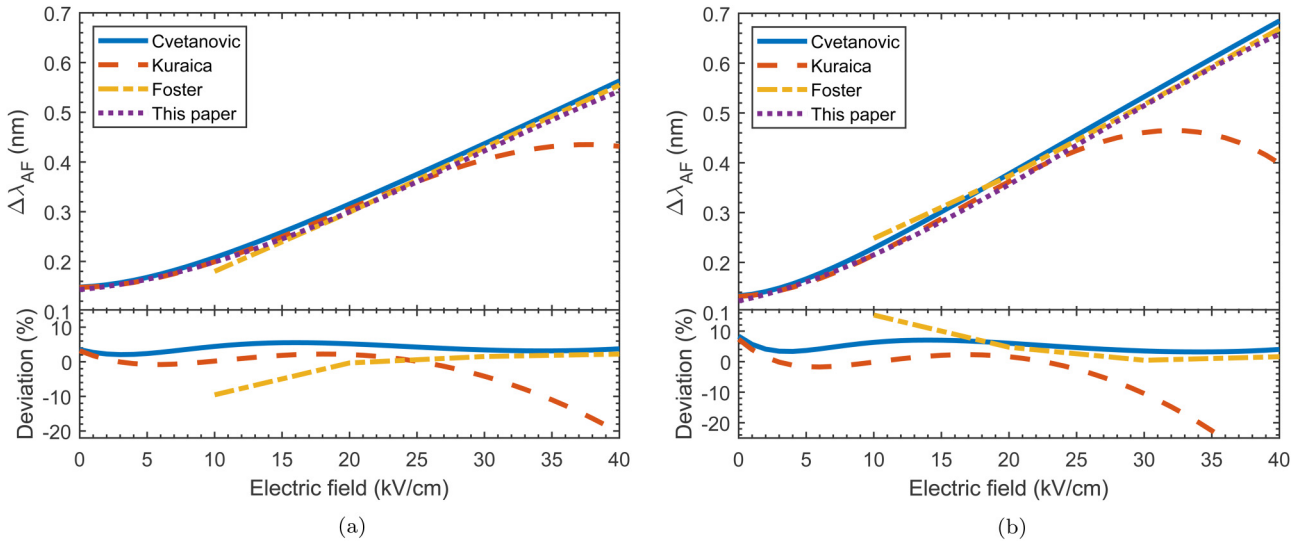

FIG. 10. Comparison of the results from this paper and the results from Cvetanovic *et al.*,[8] Kuraica,[24] and Foster[20] for the difference between the shifted allowed and forbidden line as a function of the electric field: (a) for the He I 447.1 nm line and (b) for the He I 492.2 nm line. The bottom graph shows the deviation (in percentage) of the difference between the different results and the results from this paper.

relatively large, while at higher electric fields, the deviation is less than 5%. The deviation may be explained by the difference in accuracy of the energy levels, from which $\lambda_{0,1,2,3}$ are calculated, since the energy levels in Foster's paper originate from before 1927[54] and the used energy levels in this paper from 2006[52] and 2010.[53] The results from Kuraica are only valid between 0 kV/cm and 20 kV/cm. In this region, the deviation is less than 5%, while outside this region, the deviation is large (up to 35%). The deviation of the results from Cvetanovic is up to 5% in the full range of the electric field, thus these results are in good agreement.

In general, the results from this paper are in good agreement with previous work in the electric field range where the results are valid.

APPENDIX B: SELECTING THE AXIAL COMPONENT OF THE ELECTRIC FIELD

The Stark effect is the splitting and shifting of spectral lines under the influence of an externally applied electric field.[55,56]

By choosing to measure only the light emitted with the polarization direction in the z-direction (which is parallel to the propagation direction of the ionization wave), we select only the π-component (component with $\Delta m = 0$). This will be shown in this Appendix.

In this paper, a helium plasma is studied. The helium atom has a dipole and when the atom is placed in an electric field, it will align its dipole axis with the axis of the electric field.[57] The (positive) nucleus is pushed in the direction along the electric field and the (negative) electrons in the opposite direction. On the other hand, there is the attractive force between the nucleus and the electrons, and thus an equilibrium establishes between these two forces.[57] The dipole moment $\vec{d}$ is given by[50]

$$\vec{d} = \alpha \vec{E}, \tag{B1}$$

in which α is the polarizability and $\vec{E}$ the electric field. The polarizability is a tensor for molecules, but a constant for atoms, since they are spherically symmetric.[58] For the helium atom, the value is $0.204956 \cdot 10^{-24}\,\mathrm{cm}^3$.[59] Therefore, the dipole moment of the helium atom lies parallel to the electric field.

The probability that an atom will undergo a transition from state n to n', while emitting light of polarization direction $\vec{e_j}$ into solid angle $\mathrm{d}\Omega$ is[24,48]

$$\mathrm{W}(\Omega, \mathrm{j})\mathrm{d}\Omega = \frac{e^2\omega_{nn'}^3}{2\pi\hbar c^3}\left(\vec{e_j}\cdot\vec{d}_{n'n}\right)^2 \mathrm{d}\Omega, \tag{B2}$$

in which e is the elementary charge, c the speed of light, $\omega_{nn'} = (\mathrm{E}_n - \mathrm{E}_{n'})/\hbar$ the oscillation frequency of the dipole and $\vec{d}_{n'n}$ the dipole matrix element

$$\vec{d}_{n'n} = \int \psi^* \vec{d} \psi \, \mathrm{d}\tau. \tag{B3}$$

The intensity $\mathrm{J_j}$ of this light is obtained by multiplying Eq. (B2) with the energy of a light quantum $\hbar\omega$,[24,48] yielding

$$\mathrm{J_j}\mathrm{d}\Omega = \frac{e^2\omega_{nn'}^4}{2\pi c^3}\left(\vec{e_j}\cdot\vec{d}_{n'n}\right)^2 \mathrm{d}\Omega, \tag{B4}$$

meaning that the intensity of the emitted light depends on the polarization direction.

A transition from state n to n' is only possible if $\mathrm{W}(\Omega, \mathrm{j}) \neq 0$, thus only if $\vec{d}_{n'n} \neq 0$. Calculating the different components of the matrix element gives the following. Using Eq. (B1), Eq. (B3), and $\mathrm{E_z} = \mathrm{E_0}\cos\theta$, the z-component of $\vec{d}_{n'n}$ is

$$\begin{aligned} d_{n'n}^z &= \int \psi_{n'l'm'}^* \alpha \mathrm{E_z} \psi_{nlm} \, \mathrm{d}\vec{r} \\ &= \alpha \mathrm{E_0} \int_0^\infty \mathrm{R}_{n'l'}(r)\mathrm{R}_{nl} r^2 \, \mathrm{d}r \int_0^{2\pi} \frac{1}{2\pi} \mathrm{e}^{\mathrm{i}(m-m')\phi} \, \mathrm{d}\phi \\ &\quad \int_0^\pi \mathrm{P}_{l'm'}(\theta)\cos\theta \mathrm{P}_{lm}(\theta)\sin\theta \, \mathrm{d}\theta, \end{aligned} \tag{B5}$$

with

$$\psi_{nlm} = \mathrm{R}_{nl}(r)\mathrm{P}_{lm}(\theta)\,\mathrm{e}^{\mathrm{i}m\phi}\frac{1}{\sqrt{2\pi}}. \tag{B6}$$

The integral over ϕ vanishes if $m \neq m'$, thus $m = m'$ should hold and the selection rule for m is obtained

$$\Delta m = m' - m = 0. \tag{B7}$$

For the integral over θ, the substitution of

$$\begin{aligned} \mathrm{P}_{lm}\cos\theta &= \sqrt{\frac{(l+1)^2 - m^2}{(2l+3)(2l+1)}}\mathrm{P}_{l+1m} \\ &\quad + \sqrt{\frac{l^2 - m^2}{(2l+1)(2l-1)}}\mathrm{P}_{l-1m} \end{aligned} \tag{B8}$$

in the integral and the use of

$$\int_0^\infty \mathrm{P}_{l'm'}\mathrm{P}_{lm}\sin\theta \, \mathrm{d}\theta = \delta_{ll'} \tag{B9}$$

yield that the integral vanishes unless

$$\Delta l = l' - l = \pm 1 \tag{B10}$$

holds. Therefore, Eq. (B10) is the selection rule for l. The final expressions for the matrix elements $d_{n'n}^z$ [Eq. (B5)] then

become

$$(d_z)^{n'l+1m}_{nlm} = \alpha E_0 \sqrt{\frac{(l+1)^2 - m^2}{(2l+3)(2l+1)}} R^{n'l+1}_{nl}, \tag{B11}$$

$$(d_z)^{n'l-1m}_{nlm} = \alpha E_0 \sqrt{\frac{l^2 - m^2}{(2l+1)(2l-1)}} R^{n'l-1}_{nl}, \tag{B12}$$

with

$$R^{n'l'}_{nl} = \int R_{n'l'}(r) R_{nl}(r) r^2 \mathrm{d}r. \tag{B13}$$

Thus, an electric field in the direction parallel to the axis of the jet, in this case the z-direction, will only induce transitions in the helium atom that emit linearly polarized light, i.e., transitions with $\Delta m = 0$ (the π-component).

The x and y components of $\vec{d}_{n'n}$ originate from an electric field with x and y-components. To simplify the calculation, a linear combination of $d^x_{n'n}$ and $d^y_{n'n}$ is made

$$E_x + iE_y = E_0 \sin\theta \, e^{i\phi}, \quad E_x - iE_y = E_0 \sin\theta \, e^{-i\phi}.$$

The corresponding matrix elements then become

$$\begin{aligned} d^x_{n'n} \pm i d^y_{n'n} = \frac{\alpha E_0}{2\pi} \int_0^\infty P_{l'm'}(\theta) P_{lm}(\theta) \sin^2\theta \, \mathrm{d}\theta \\ \int_0^\infty R_{n'l'}(r) R_{nl}(r) r^2 \, \mathrm{d}r \\ \int_0^\infty e^{\pm i\phi} e^{-i(m-m')\phi} \, \mathrm{d}\phi. \end{aligned} \tag{B14}$$

The integral over ϕ again vanishes unless $m' - m \pm 1 = 0$, which yields the selection rule for m

$$\Delta m = m' - m = \pm 1. \tag{B15}$$

For the θ part, substituting

$$\begin{aligned} P_{lm} \sin\theta = \pm \sqrt{\frac{(l \pm m + 1)(l \pm m + 2)}{(2l+1)(2l+3)}} P_{l+1m\pm1} \\ \mp \sqrt{\frac{(l \mp m)(l \mp m - 1)}{(2l+1)(2l-1)}} P_{l-1m\pm1} \end{aligned} \tag{B16}$$

and using Eq. (B9) again yields the selection rule for l

$$\Delta l = l' - l = \pm 1. \tag{B17}$$

The final matrix elements $d^x_{n'n} \pm i d^y_{n'n}$ then are

$$\begin{aligned} &(d_x \pm i d_y)^{n'l+1m\pm1}_{nlm} \\ &\quad = \pm \alpha E_0 \sqrt{\frac{(l \pm m + 1)(l \pm m + 2)}{(2l+1)(2l+3)}} R^{n'l+1}_{nl}, \end{aligned} \tag{B18}$$

$$\begin{aligned} &(d_x \pm i d_y)^{n'l-1m\pm1}_{nlm} \\ &\quad = \mp \alpha E_0 \sqrt{\frac{(l \mp m)(l \mp m - 1)}{(2l+1)(2l-1)}} R^{n'l-1}_{nl}, \end{aligned} \tag{B19}$$

with $R^{n'l'}_{nl}$ as in Eq. (B13). Thus, an electric field in the direction perpendicular to the axis of the jet, thus in the xy-plane, will only induce transitions in the helium atom that emit circularly polarized light, i.e., transitions with $\Delta m = \pm 1$ (the σ-component).

REFERENCES

[1] T. von Woedtke, S. Reuter, K. Masur, and K.-D. Weltmann, Phys. Rep. **530**, 291 (2013).
[2] D. Graves, Phys. Plasmas **21**, 080901 (2014).
[3] A. Sobota, O. Guaitella, G. B. Sretenović, I. B. Krstić, V. V. Kovačević, A. Obrusník, Y. N. Nguyen, L. Zajíčková, B. M. Obradović, and M. M. Kuraica, Plasma Sources Sci. Technol. **25**, 065026 (2016).
[4] I. H. Hutchinson, Plasma Phys. Controlled Fusion **44**, 2603 (2002).
[5] H.-J. Kunze, *Springer Series on Atomic, Optical, and Plasma Physics*, 1st ed. (Springer Berlin Heidelberg, Berlin, Heidelberg, 2009), Vol. 56.
[6] G. L. Majstorović, N. V. Ivanović, N. M. Šišović, S. Djurović, and N. Konjević, Plasma Sources Sci. Technol. **22**, 045015 (2013).
[7] N. V. Ivanović, N. M. Šišović, D. Spasojević, and N. Konjević, J. Phys. D Appl. Phys. **50**, 125201 (2017).
[8] N. Cvetanović, M. M. Martinović, B. M. Obradović, and M. M. Kuraica, J. Phys. D Appl. Phys. **48**, 205201 (2015).
[9] B. M. Goldberg, I. Shkurenkov, S. O'Byrne, I. V. Adamovich, and W. R. Lempert, Plasma Sources Sci. Technol. **24**, 35010 (2015).
[10] P. Böhm, M. Kettlitz, R. Brandenburg, H. Höft, and U. Czarnetzki, Plasma Sources Sci. Technol. **25**, 54002 (2016).
[11] M. S. Simeni, E. Baratte, C. Zhang, K. Frederickson, and I. V. Adamovich, Plasma Sources Sci. Technol. **27**, 015011 (2018).
[12] M. S. Simeni, B. Goldberg, I. Gulko, K. Frederickson, and I. V. Adamovich, J. Phys. D Appl. Phys. **51**, 01LT01 (2018).
[13] B. M. Goldberg, T. L. Chng, A. Dogariu, and R. B. Miles, Appl. Phys. Lett. **112**, 064102 (2018).
[14] M. S. Simeni, Y. Tang, K. Frederickson, and I. V. Adamovich, Plasma Sources Sci. Technol. **27**, 104001 (2018).
[15] E. V. Barnat and K. Frederickson, Plasma Sources Sci. Technol. **19**, 055015 (2010).
[16] E. V. Barnat and A. Fierro, J. Phys. D Appl. Phys. **50**, 14LT01 (2017).
[17] A. Sobota, O. Guaitella, and E. Garcia-Caurel, J. Phys. D Appl. Phys. **46**, 372001 (2013).
[18] E. Slikboer, O. Guaitella, and A. Sobota, Plasma Sources Sci. Technol. **25**, 03LT04 (2016).
[19] S. S. Ivković, G. B. Sretenović, B. M. Obradović, N. Cvetanović, and M. M. Kuraica, J. Phys. D Appl. Phys. **47**, 055204 (2014).
[20] J. S. Foster, Proc. R. Soc. Lond. Ser. A **117**(775), 137 (1927).
[21] I. Videnović, N. Konjević, and M. Kuraica, Spectrochim. Acta Part B **51**, 1707 (1996).
[22] M. Kuraica, N. Konjević, and I. Videnović, Spectrochim. Acta Part B **52**, 745 (1997).
[23] M. M. Kuraica and N. Konjević, Appl. Phys. Lett. **70**, 1521 (1997).

[24]M. M. Kuraica, "Razvoj novih spektroskopskih metoda za dijagnostiku tinjavog pražnjenja," Ph.D. thesis (University of Belgrade, 1998).
[25]G. B. Sretenović, I. B. Krstić, V. V. Kovaćević, B. M. Obradović, and M. M. Kuraica, Appl. Phys. Lett. **99**, 2011 (2011).
[26]E. Slikboer, E. Garcia-Caurel, O. Guaitella, and A. Sobota, Plasma Sources Sci. Technol. **26** (2017).
[27]A. Sobota, O. Guaitella, and A. Rousseau, Plasma Sources Sci. Technol. **23**, 025016 (2014).
[28]Maxim: Peak fitting to Voigt profile, see https://nl.mathworks.com/matlabcentral/ fileexchange/52321-peak-fitting-to-either-voigt-or-lognormal-line-shapes.
[29]P. Olszewski, E. Wagenaars, K. McKay, J. W. Bradley, and J. L. Walsh, Plasma Sources Sci. Technol. **23**, 015010 (2014).
[30]G. B. Sretenović, O. Guaitella, A. Sobota, I. B. Krstić, V. V. Kovačević, B. M. Obradović, and M. M. Kuraica, J. Appl. Phys. **121**, 123304 (2017).
[31]D. Riès, G. Dilecce, R. Robert, P. F. Ambrico, S. Dozias, and J.-M. Pouvesle, J. Phys. D Appl. Phys. **47**, 275401 (2014).
[32]LaPointe, Electrical properties of plastics, see http://members.tm.net/lapointe/Plastics.htm.
[33]S. Gu, T. Lin, and T. Lasri, Meas. Sci. Technol. **28**, 014014 (2017).
[34]F. Tanaka, P. Mallikarjunan, C. Kim, and Y. Hung, J. Jpn. Soc. Agric. Mach. Food Eng. **62**, 109 (2000).
[35]W. M. Haynes, *CRC Handbook of Chemistry and Physics*, 95th ed. (CRC Press, 2014).
[36]S. Sarang, S. K. Sastry, and L. Knipe, J. Food. Eng. **87**, 351 (2008).
[37]A. J. K. A. Z. Al-Ramadhan and A. Hashim, AIP Conf. Proc. **180**, 1400 (2011).
[38]S. A. Norberg, E. Johnsen, and M. J. Kushner, J. Appl. Phys. **118**, 013301 (2015).
[39]B. L. M. Klarenaar, O. Guaitella, R. Engeln, and A. Sobota, Plasma Sources Sci. Technol. **27**, 085004 (2018).
[40]D. Breden and L. L. Raja, Plasma Sources Sci. Technol. **23**, 065020 (2014).
[41]S. A. Norberg, E. Johnsen, and M. J. Kushner, J. Phys. D Appl. Phys. **49**, 185201 (2016).
[42]W. Yan and D. J. Economou, J. Appl. Phys. **120**, 123304 (2016).
[43]P. Viegas, F. Péchereau, and A. Bourdon, Plasma Sources Sci. Technol. **27**, 025007 (2018).
[44]T. Gerling, A. V. Nastuta, R. Bussiahn, E. Kindel, and K.-D. Weltmann, Plasma Sources Sci. Technol. **21**, 034012 (2012).
[45]T. Darny, J.-m. Pouvesle, J. Fontane, L. Joly, S. Dozias, and E. Robert, Plasma Sources Sci. Technol. **26**, 105001 (2017).
[46]K. McKay, J. S. Oh, J. L. Walsh, and J. W. Bradley, J. Phys. D Appl. Phys. **46**, 464018 (2013).
[47]D. J. Griffiths and E. G. Harris, *Introduction to Quantum Mechanics*, 2nd ed. (Pearson Prentice Hall, 2005).
[48]H. A. Bethe and E. E. Salpeter, *Quantum Mechanics of One- and Two-Electron Atoms* (Springer Berlin Heidelberg, Berlin, Heidelberg, 1957).
[49]D. D. Fitts, *Principles of Quantum Mechanics*, 1st ed. (Cambridge University Press, Cambridge, 1999).
[50]D. J. Griffiths, *Introduction to Electrodynamics*, 4th ed. (Pearson, 2013).
[51]W. Demtröder, *Atoms, Molecules and Photons, Graduate Texts in Physics* (Springer Berlin Heidelberg, Berlin, Heidelberg, 2010).
[52]D. C. Morton, Q. Wu, and G. W. Drake, Can. J. Phys. **84**, 83 (2006).
[53]A. Kramida, Atomic Data Nucl. Data Tables **96**, 586 (2010).
[54]A. Fowler, *Report on Series in Line Spectra* (Fleetway Press, Ltd., 1922).
[55]J. Stark, Ann. Phys. **348**, 965 (1914).
[56]J. Stark and G. Wendt, Ann. Phys. **348**, 983 (1914).
[57]J. Stark, Ann. Phys. **353**, 210 (1915).
[58]K. D. Bonin and V. V. Kresin, *Electric-dipole Polarizabilities of Atoms, Molecules, and Clusters* (World Scientific, Singapore, 1997).
[59]D. R. Lide, *CRC Handbook of Chemistry and Physics*, 84th ed. (CRC Press, 2003).